



Charge state distribution of ^{86}Kr in hydrogen and helium gas charge strippers at 2.7 MeV/nucleon

H. Kuboki,* H. Okuno, H. Hasebe, N. Fukunishi, E. Ikezawa, H. Imao,
O. Kamigaito, and M. Kase

RIKEN Nishina Center for Accelerator-Based Science, Wako, Saitama 351-0198, Japan
(Received 28 May 2014; published 2 December 2014)

The charge state distributions of krypton (^{86}Kr) with an energy of 2.7 MeV/nucleon were measured using hydrogen (H_2) and helium (He) gas charge strippers. A differential pumping system was constructed to confine H_2 and He gases to a thickness sufficient for the charge state distributions to attain equilibrium. The mean charge states of ^{86}Kr in H_2 and He gases attained equilibrium at 25.1 and 23.2, respectively, whereas the mean charge state in N_2 gas at equilibrium was estimated to be less than 20. The charge distributions are successfully reproduced by the cross sections of ionization and electron capture processes optimized by a fitting procedure.

DOI: 10.1103/PhysRevSTAB.17.123501

PACS numbers: 29.20.dg, 29.25.Pj, 34.50.Fa

I. INTRODUCTION

The charge states of heavy-ion beams play an important role in the performance of heavy-ion accelerators [1–5]. Figure 1 shows the acceleration scheme of medium-mass ions such as calcium and krypton (Kr) at the RIKEN RI Beam Factory (RIBF) [6,7]. Kr ions are extracted from the RIKEN 18-GHz electron cyclotron resonance (ECR) ion source [8], and they are successively accelerated up to the final energy of 345 MeV/nucleon using the RIKEN heavy-ion linac (RILAC) [9], the RIKEN ring cyclotron (RRC) [10,11], an intermediate-stage ring cyclotron (IRC) [12], and a superconducting ring cyclotron (SRC) [13,14]. Two charge stripper sections are placed downstream of the RILAC and RRC. The initial charge states of the Kr ions extracted from the ECR ion source are 18+ to 20+ depending on the mass numbers of the accelerated Kr ions (78–86).

The Kr beams are accelerated up to 2.7 MeV/nucleon using the RILAC, and they are transported to the first charge stripper located at the exit of the RILAC. Carbon foils (C-foils) with thicknesses in the range of 40–80 $\mu\text{g}/\text{cm}^2$ [15] are generally utilized as the first charge stripper to strip the charge of the ^{86}Kr beam to 26+, which is the lowest acceptable charge state for ^{86}Kr acceleration as determined by the K -value of the subsequent cyclotron RRC ($K = 540$ MeV). The charge states of heavy ions in solid materials have been intensively studied, and a large amount of data for Kr over the energy range of 0.01–100 MeV/nucleon is available in Refs. [16–22]. The charge

distributions and equilibrium charge state of ^{86}Kr in C-foils at 2.7 MeV/nucleon were also measured at RIBF [23]. The results indicated that a sufficiently high mean charge state of 26.1 was obtained, and the fraction of $^{86}\text{Kr}^{26+}$ was 35%.

The stripping energy E at the second charge stripper is $E = 46$ MeV/nucleon. The charge state used for subsequent acceleration has not been determined explicitly, but it should be higher than 32+, which is the lowest acceptable charge state of the SRC ($K = 2600$ MeV). Practically, the charge state for acceleration is determined considering the fraction of the desired charge state and emittance growth after the beam passes through the stripper. The charge state of 34+ is one of the target charge states that can be obtained by using a C-foil charge stripper with a thickness in the range of 0.5–1 mg/cm^2 [24]. The fraction of Kr^{34+} is 60–65% depending on the stripper thickness. As mentioned in Ref. [24], the fraction of 36+ attains 80% upon using C-foils with thicknesses over 10 mg/cm^2 . However, the emittance growth of the stripped beam is estimated to be considerably large, and beam loss would increase beyond the permissible limits.

We focus on the first charge stripper since it locates far upstream from the final cyclotron (SRC) and its lifetime greatly affects the beam availability. Inherently, C-foil

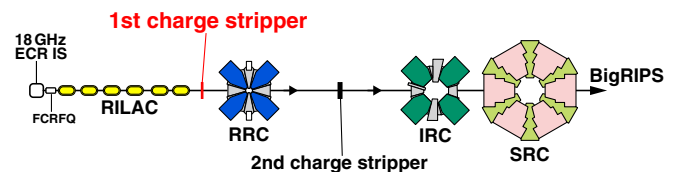


FIG. 1. Acceleration scheme of Kr-ion beams at RIBF. The ^{86}Kr beams are accelerated by means of a linear accelerator (RILAC) and three cyclotrons (RRC, IRC, and SRC). The first and second charge strippers are located downstream of the RILAC and RRC, respectively.

*kuboki@riken.jp

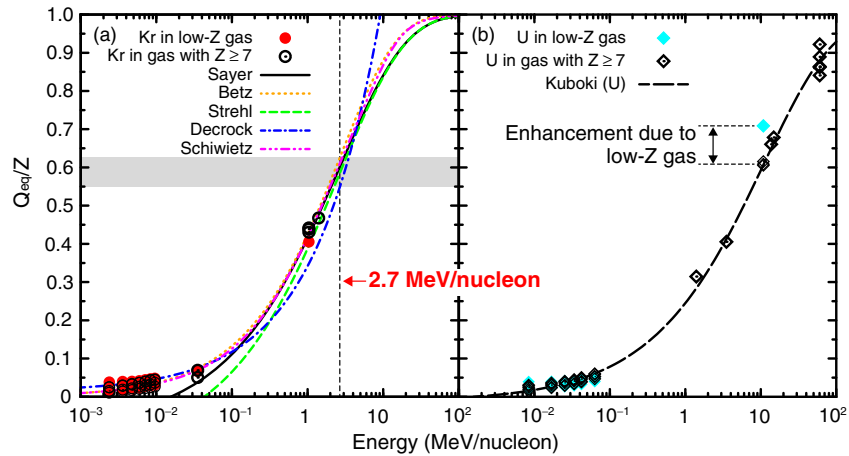


FIG. 2. The data of equilibrium charge state Q_{eq} divided by the projectile atomic number Z for (a) Kr and (b) U ions in gas media. (a) Solid and open circles represent Kr data for low- Z [18,33], and heavier [18,19,33] gas media, respectively. Solid, dotted, dashed, dash-dotted, and dash-two-dotted curves represent Q_{eq}/Z in gas media as predicted by the empirical formulas proposed by Sayer [28], Betz [29], Strehl [30], Decrock [31], and Schiwietz [32], respectively. (b) Solid and open diamonds represent the Q_{eq}/Z data of U in low- Z (He) [34] and heavier ($Z \geq 7$) [16,18,19,22,35–37] gas media, respectively.

strippers have a finite lifetime to provide stable beams with a constant required intensity.

Gas charge strippers have been suggested as a possible candidate in the light of their durability. However, as is commonly known, the charge states in gas media attain far lower values than with C-foils because of the *density effect* [16,25–27]. Figure 2(a) shows the plots of the semi-empirical formulas to predict the mean charge states of ^{86}Kr in gas media at equilibrium (Q_{eq}) divided by the projectile atomic number Z (Q_{eq}/Z). The predicted values are plotted as a function of the projectile energy E . The figure includes the empirical formulas for predicting charge states in gas media as proposed by Sayer [28] (solid line), Betz [29] (dotted line), Strehl [30] (dashed line), Decrock [31] (dash-dotted line), and Schiwietz [32] (dash-two-dotted line). The predicted values of Q_{eq} vary from 19.7 to 22.5, which are far less than the target value of 26. The data of Kr in gases with $Z \geq 7$, such as nitrogen (N_2), neon, or argon, are also plotted using open circles [18,19,33].

Recently, charge strippers using gases with small atomic numbers (low- Z) such as hydrogen (H_2) or helium (He) have been found to provide considerably higher charge states among gases [34,38]. A datum of the equilibrium charge state of uranium (U) in He gas is indicated by the solid diamond at 10.8 MeV/nucleon in Fig. 2(b) [34]. The Q_{eq} data of U in heavier gases with $Z \geq 7$ are indicated by open diamonds [16,18,19,22,35–37] along with the plot of the semi-empirical formula (long-dashed line) [36]. The Q_{eq} of U in He is greater by almost 10 ($Q_{\text{eq}}/Z \sim 0.1$) when compared with those of other gases such as N_2 , etc. On the other hand, we note that no difference in equilibrium charge states is observed in the low-energy region ($E < 0.1$ MeV/nucleon) between He and other heavier gases. Similarly, in the Kr case, for which the data

corresponding to low- Z gas [18,33] are indicated by solid circles in Fig. 2(a), the equilibrium charge states obtained with low- Z gases and those for heavier gases show no difference even in the energy region of $E \lesssim 1.0$ MeV/nucleon. However, since Q_{eq}/Z increases drastically up to the energy region $E \sim 10$ MeV/nucleon, Q_{eq} in H_2 or He gases might become higher than those for other gases at 2.7 MeV/nucleon.

In the present study, we measured the charge state distributions of ^{86}Kr at 2.7 MeV/nucleon using H_2 and He gas strippers with different thicknesses. Additional data were obtained for the charge state distribution of N_2 gas to evaluate the difference between low- Z gases and other gases.

II. GAS CHARGE STRIPPING SYSTEM

We constructed a prototype of a windowless gas charge stripping system in a beam line based on the basic design of the differential pumping system [34,39,40]. Figures 3 and 4 show the overview of the beam line and its detailed diagram, respectively. The gas charge stripper was installed between the X51 section and the X-Rebuncher (XReb). Figure 5 shows the schematic of this system along with differential pumping speeds. The target region was designated as stage 1 and its physical length was 100 cm. The target gas was injected into stage 1, and its two neighboring stages were prepared for differential pumping. The two differentially pumped stages were located both upstream and downstream of stage 1, and they were designated as stages U2 and U3 for upstream and D2 and D3 for downstream, respectively. Stages U3 and D3 were connected to the beam-line chambers X51a and X51b, respectively. A 10-cm-long tube with 4-mm inner diameter was installed between each stage for reducing the gas

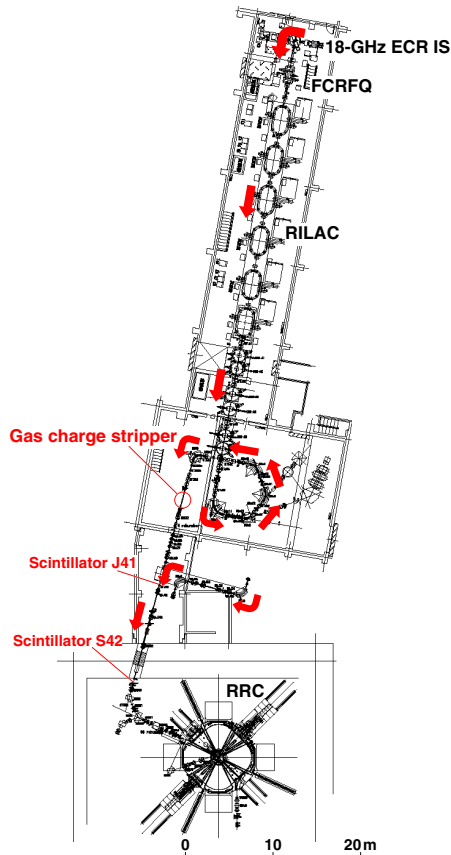


FIG. 3. The beam line from the RILAC to the RRC. The gas charge stripper is located downstream of the RILAC.

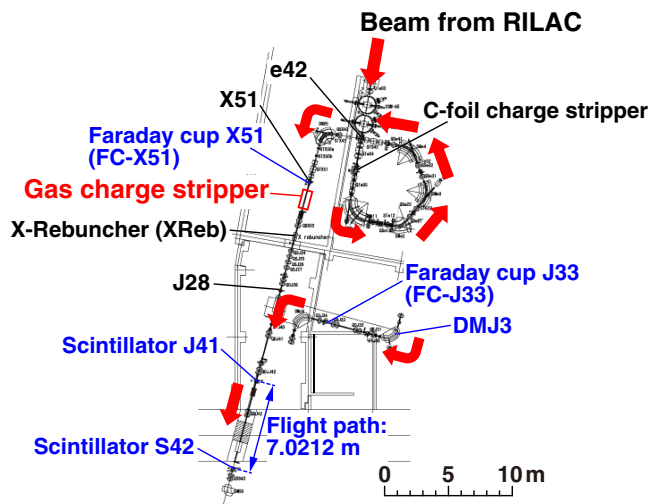


FIG. 4. Schematic of the gas charge stripper and its surroundings. The gas stripper is located between the X51 and X-Rebuncher (XReb) sections. We measured the gas pressures at sections e42, X51, XReb, and J28. The beam intensity upstream of the gas charge stripper was measured using a Faraday cup (FC-X51). The charge states of the stripped beams were analyzed using a DMJ3 dipole magnet. The beam intensity downstream of the DMJ3 was measured using a Faraday cup (FC-J33).

throughput outside of the gas target region. Three tubes were located upstream and downstream of stage 1, i.e., the Kr beam passed through a total of six tubes.

The pressure at stage 1 (P_1) was measured by two gauges located upstream (P_{U1}) and downstream (P_{D1}). The pressures at stages U2 (D2) and U3 (D3) are indicated by $P_{U2(D2)}$ and $P_{U3(D3)}$, respectively. We also measured the gas pressures at sections X51, e42, XReb, and J28 (see Fig. 4) and their corresponding pressures were designated P_{X51} , P_{e42} , P_{XReb} , and P_{J28} , respectively. The sections X51 and e42 were 1.0 m and 8.0 m upstream from the center of stage 1, respectively, while the sections XReb and J28 were 3.1 m and 7.5 m downstream, respectively.

Since the gas charge stripper is operated at a beam line, the pressure in stages other than stage 1 are expected to fall rapidly when the pressure P_1 is maintained constant. The stages U2 and D2 were evacuated by a pair of mechanical booster pumps (MBPs, Edwards, EH500) with a total evacuation speed of $730 \text{ m}^3/\text{h}$, i.e., $365 \text{ m}^3/\text{h}$ for each stage. The stages U3 and D3 were evacuated by a turbomolecular pump (TMP) with a pumping speed of $1980 \text{ m}^3/\text{h}$ (SHIMADZU EMIT CO., TMP-550L). The chambers X51a and X51b were evacuated by a TMP with a pumping speed of $792 \text{ m}^3/\text{h}$ (Osaka Vacuum, TG220F-CAB). The back pumps for the MBPs and TMPs were rotary pumps with an evacuation speed of $4.5 \text{ m}^3/\text{h}$ (Alcatel 2004A).

The target gas was injected through a mass flow controller (MKS, Type 1579A) and gas flow was tuned so that the pressures P_{U1} and P_{D1} reached desired values. P_{U1} and P_{D1} were measured by a baratron transducer (MKS, 627B) and a sapphire capacitance diaphragm gauge (Tem-Tech Lab., SCM2100), respectively. The pressures P_{U2} and P_{D2} were measured by means of MicroPirani™/Piezo loadlock transducers (MKS, 901P). The pressures P_{U3} , P_{D3} , P_{X51} , P_{e42} , P_{XReb} , and P_{J28} were measured using cold cathode gauges (Pfeifer IKR060) in the low-pressure range ($< 0.1 \text{ Pa}$) or measured by constant-temperature-type Pirani gauges (Pfeifer, TPR010) in the higher-pressure region ($> 0.1 \text{ Pa}$). Since all pressure values indicated by gauges except for P_{U1} and P_{D1} depended on the gas species, their values were adequately corrected [41].

A. Offline pressure test

We performed an offline test to evaluate the maximum possible value of P_1 with H_2 and He gas injection. The results are shown in Figs. 6 and 7 for H_2 and He gases, respectively. Pressures $P_{U2(D2)}$, $P_{U3(D3)}$, $P_{X51(XReb)}$, and $P_{e42(J28)}$ are plotted as functions of P_{U1} (P_{D1}) in Fig. 6(a) [Fig. 6(b)] and indicated by open circles (open triangles), solid circles (solid triangles), crosses (x-marks), and open squares (solid squares), respectively. The required maximum pressure at the target region was determined by the gas thickness required for the charge states to attain equilibrium. In the case of a C-foil, the most probable

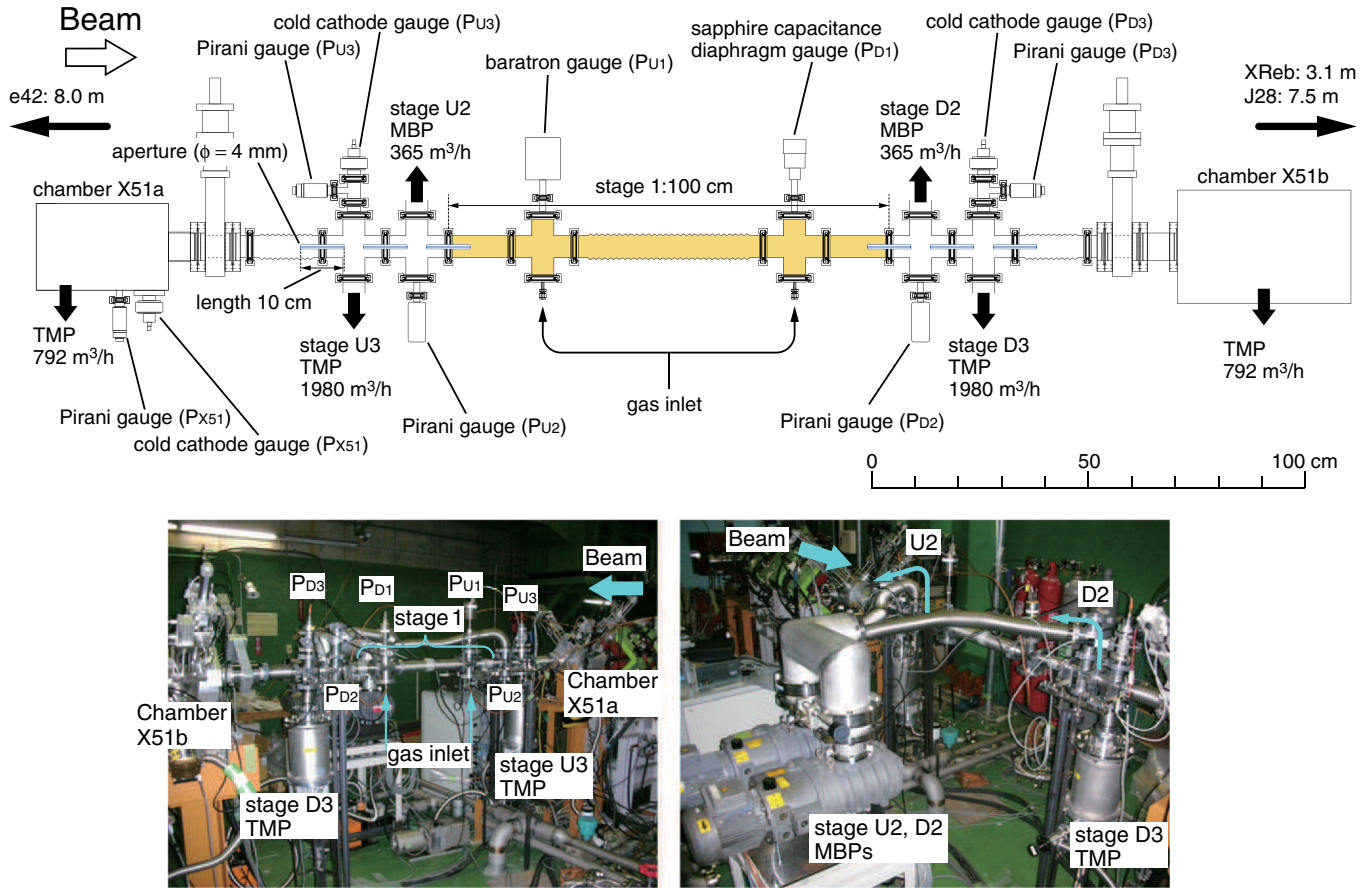


FIG. 5. Schematic of the gas charge stripper with the differential pumping system. Gases are injected into the target region (stage 1) located at the center. The length of the target region is 100 cm. Other stages are also shown along with the pumping speeds of their respective attached pumps. Three tubes with an inner aperture of 4 mm in diameter and length of 10 cm are placed at the entrance and exit of the target region.

charge state attains equilibrium at a thickness of $80 \mu\text{g}/\text{cm}^2$ [23]. On the assumption that the gas thickness required for equilibrium is the same as that required for equilibrium using carbon, the required maximum pressure for H_2 and He are 1 kPa and 0.5 kPa, respectively, considering the physical length of the gas target region (100 cm). On the other hand, the maximum pressure was limited by the permissible value of the safety interlock for vacuum that is applied during a beam transport operation. The permissible value was 4×10^{-3} Pa, i.e., no beam can be operational for pressures greater than this value. In the case of H_2 , P_{e42} and P_{J28} were below 4×10^{-3} Pa when P_1 ($\approx P_{U1} \approx P_{D1}$) was maintained lower than 1.1 kPa. The interlock was applied by the values measured at P_{e42} and P_{J28} in the case of H_2 gas operation. With regard to the case of He , P_{U2} (D2), P_{U3} (D3), and P_{X51} (XR**e**b) are plotted as functions of P_{U1} (P_{D1}) in Fig. 7(a) [Fig. 7(b)] and indicated by open circles (open triangles), solid circles (solid triangles), and crosses (x-marks), respectively. Since P_{X51} and $P_{XR**e**b}$ were sufficiently lower than the admissible value up to $P_1 = 1.8$ kPa, the interlock was applied by P_{X51} and $P_{XR**e**b}$, and the curves corresponding to P_{e42} and P_{J28} are not plotted in Fig. 7.

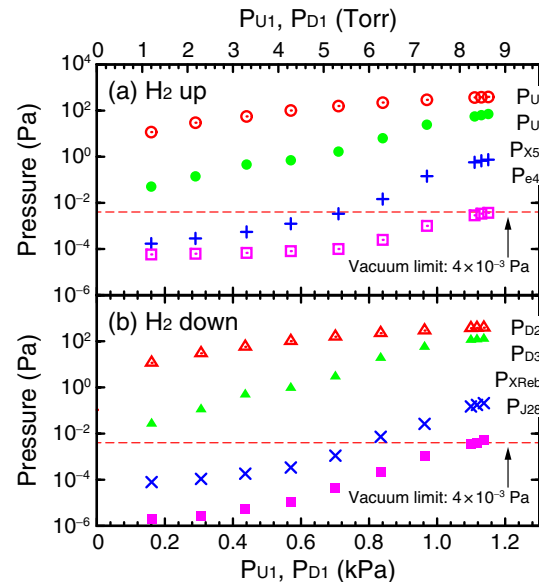


FIG. 6. The pressure at each stage is plotted as a function of P_1 for H_2 gas. (a) The pressures at the stages upstream of the gas stripper (P_{U2} , P_{U3} , P_{X51} , and P_{e42}) as a function of P_{U1} . (b) The pressures downstream of the gas stripper (P_{D2} , P_{D3} , $P_{XR**e**b}$, and P_{J28}) as a function of P_{D1} .

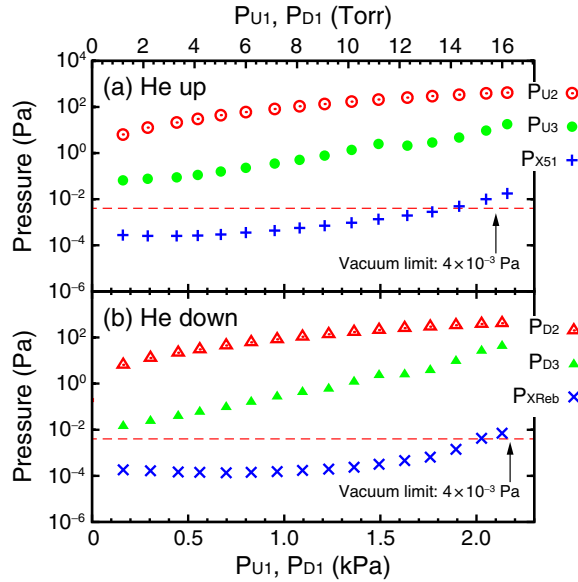


FIG. 7. The pressure at each stage is plotted as a function of P_1 for He gas. (a) The pressures at the stages upstream of the gas stripper (P_{U2} , P_{U3} , and P_{X51}) as a function of P_{U1} . (b) The pressures downstream of the gas stripper (P_{D2} , P_{D3} , and P_{XReb}) as a function of P_{D1} . Those at P_{e42} and P_{J28} are not plotted since the pressures P_{X51} and P_{XReb} are below the permissible value of 4×10^{-3} Pa when maintaining P_1 up to 1.8 kPa.

III. EXPERIMENTS

A. Krypton beam acceleration and transport

A series of experiments was performed at the RIKEN RIBF in February 2012 and February 2013 by accelerating ^{86}Kr beams up to 2.7 MeV/nucleon. The ^{86}Kr beams were accelerated using the RILAC at a rf-frequency of 36.5 MHz. The $^{86}\text{Kr}^{20+}$ ions with an intensity of 11–12 $e\mu\text{A}$ were provided by the 18-GHz ECRIS and were transported to the gas charge stripper. The incident beam intensities were measured to be 650–750 enA (33–38 pA) with an attenuation of 1/10 using a Faraday cup (FC-X51) placed upstream of the gas charge stripper. The beam spot size was 5 mm in diameter at the just upstream of the system. Since this gas stripping system was a prototype, we had no focusing element such as quadrupole or solenoid magnet to transport the beam adequately through the system. Moreover, as written in Sec. II, six tubes with an inner diameter of 4 mm were used for reduction of gas throughput to enhance the differential pumping efficiency in a limited space. Therefore, the beam was collimated by these six narrow tubes with a total length of 2 m, which corresponded to a beam transmission efficiency of 3%.

The charge state was analyzed by means of the dipole magnet DMJ3. The magnetic field of the DMJ3 was corrected by considering the energy loss in the gas. The intensities of the stripped beams were measured using a Faraday cup (FC-J33) downstream of DMJ3.

A pair of plastic scintillation counters were used to measure the energy of the beam via the time-of-flight (TOF) technique [42]. They were located at sections J41 (SC-J41) and S42 (SC-S42), as shown in Fig. 4. The flight path length between SC-J41 and SC-S42 was 7.0212 m.

B. Gas thickness calibration

In order to determine the effective thickness of the gas target region, the relationship between P_1 and the energy loss of the beams was determined by means of the TOF technique using the pair of scintillation counters SC-J41 and SC-S42. The time differences between the signals of one scintillation counter and rf signals sampled by 1/6 were measured at SC-J41 and SC-S42. Figures 8(a) and (b) show the typical time spectra of the SC-J41 and SC-S42, respectively, when using a C-foil with a thickness $10 \mu\text{g}/\text{cm}^2$. Each spectrum has six peaks, and the time difference between adjacent peaks τ_{rf} is 27.4 ns ($= 1/f$, where f denotes the rf-frequency $f = 36.5$ MHz). The error bars in the spectra represent the statistical uncertainty. Each peak was fitted by a Gaussian function (solid curve) to determine the center of the peak. The arrival times at each scintillation counter were defined as these central values. The arrival times at the SC-J41 and SC-S42 are denoted by t_{J41} and t_{S42} , respectively. The TOF of the beam t_{TOF} is written as

$$t_{\text{TOF}} = k\tau_{\text{rf}} + (t_{J41} - t_{S42}), \quad (1)$$

where $k = 11$ denotes the wave number of the bunch clock. The velocity of the beam is calculated from the expression $v = L/t_{\text{TOF}}$, where v and L denote the velocity of the beam and the flight path length between SC-J41 and SC-S42 (7.0212m), respectively. The kinetic energy E of the beam is calculated from the relation $\gamma = 1 + E/(m_u c^2)$, where γ ,

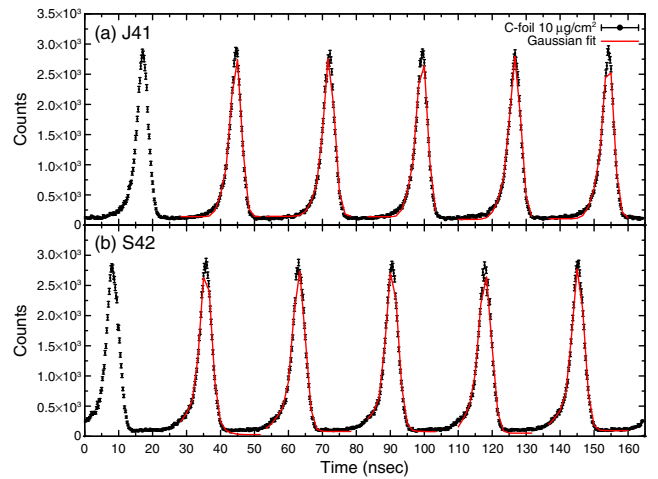


FIG. 8. Typical TOF spectra of (a) SC-J41 and (b) SC-S42 for a C-foil with a thickness of $10 \mu\text{g}/\text{cm}^2$. Gaussian functions are fitted to each peak to determine the center (arrival time).

m_u , and c denote the Lorentz factor, atomic mass unit of 931.5 MeV/ c^2 , and light velocity, respectively.

First, the TOF spectra were measured using C-foils with different thicknesses to determine the energy of the incident beam. The maximum magnetic rigidity of the magnet DMJ3 was 0.96 T m (1.2 T \times 0.8 m), which meant that a charge state of 21+ or higher was required to bend ^{86}Kr beams at 2.7 MeV/nucleon. Therefore, the incident $^{86}\text{Kr}^{20+}$ beam could not be transported beyond the DMJ3, and consequently, $^{86}\text{Kr}^{24+}$ beams were transported to SC-J41 and SC-S42 after stripping by a C-foil with known thickness values of 10, 40, and 80 $\mu\text{g}/\text{cm}^2$. Figure 9 shows the beam energies after exiting the C-foils as a function of the C-foil thickness. The error bars represent the uncertainties of the energy and the errors are attributed to the uncertainty of the arrival time obtained in the fitting procedure. The incident beam energy was estimated to be 2.672 ± 0.019 MeV/nucleon by extrapolation of the fitted linear function to zero thickness.

The spectra were obtained in the cases of H_2 , He, and N_2 gas injections at different values of P_1 . The energy loss was calculated from the difference between the case of no gas injection and the case of gas injection. The thickness of the gas medium was estimated by energy loss calculations using the ATIMA [43] package installed in LISE++ [44]. The relationships between the gas thickness and the gas pressure P_1 are shown in Fig. 10. The data for H_2 , He, and N_2 gas injections are represented by solid circles, open circles, and solid triangles, respectively. The uncertainties in thickness include the errors of the beam energy with gas injections along with the uncertainties of the incident beam energy. The data were fitted by linear functions represented by solid, dotted, and dashed lines for H_2 , He, and N_2 gas injections, respectively. The thickness of the gas charge stripper was calculated from these functions. The

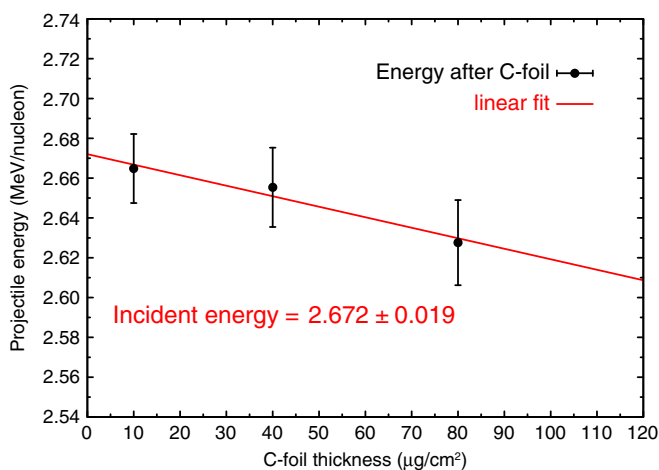


FIG. 9. Beam energies after exiting C-foils with thicknesses 10, 40, and 80 $\mu\text{g}/\text{cm}^2$. The incident energy was estimated by the extrapolation of the fitted linear function to zero. The incident energy E was determined to be 2.672 ± 0.019 MeV/nucleon.

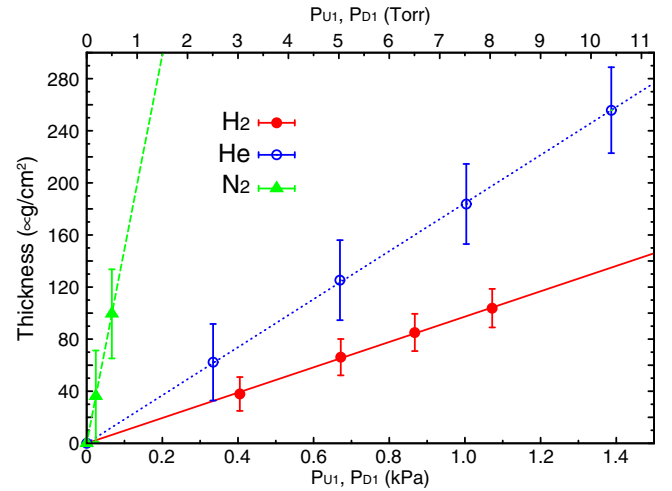


FIG. 10. Gas thickness estimated from the energy loss measurement plotted as a function of P_1 . The data for H_2 , He, and N_2 gas injections are represented by solid circles, open circles, and solid triangles, respectively. The fitting functions are represented by solid, dotted, and dashed lines for H_2 , He, and N_2 gas injections, respectively.

background pressure in the case of no gas injection was 3.6 Pa, which corresponded to an uncertainty of 3×10^{-3} MeV/nucleon at most in comparison with the pressures of H_2 or He. This background-pressure contribution is considered negligible in this study.

IV. RESULTS

A. Charge state distribution

The charge state distributions of ^{86}Kr measured using H_2 and He gas charge strippers with different thicknesses are shown in Fig. 11. The data of the fractions calculated for (a) H_2 , (b) He, and (c) N_2 are plotted in the figure. The data for H_2 gas with thicknesses of 10.3, 22.7, 45.6, 67.7, and 106.8 $\mu\text{g}/\text{cm}^2$ are denoted by asterisks, open triangles, open circles, open squares, and open diamonds, respectively. The data for He gas with thicknesses of 15.7, 29.3, 59.2, 124.0, and 247.1 $\mu\text{g}/\text{cm}^2$ are denoted by asterisks, open triangles, open circles, open squares, and open diamonds, respectively. The data for N_2 gas with thicknesses of ~ 10 , ~ 40 , ~ 800 , and ~ 1200 $\mu\text{g}/\text{cm}^2$ are denoted by asterisks, open triangles, open circles, and open squares, respectively. As shown in Fig. 11(c), the complete range of charge state distributions in N_2 gas was not obtained because of the magnetic rigidity of the analyzing DMJ3 magnet. Charge state distributions at energies considerably lower than 2.7 MeV/nucleon were obtained below 20+, for which the corresponding N_2 gas thickness values were more than 800 $\mu\text{g}/\text{cm}^2$. However, these thickness values had a large uncertainty of more than 30%. Therefore, the charge distribution in N_2 gas at equilibrium was not obtained correctly.

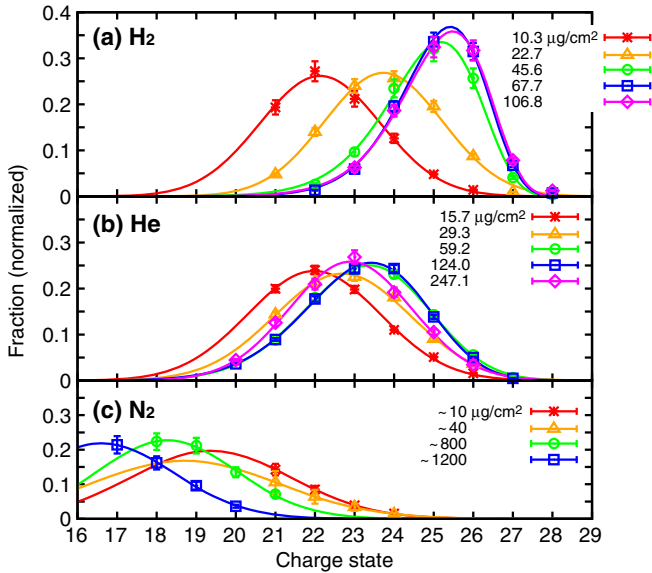


FIG. 11. Charge state distributions of ^{86}Kr . The data of the fractions calculated for (a) H_2 , (b) He , and (c) N_2 are plotted. (a) The data for H_2 gas with thicknesses of 10.3, 22.7, 45.6, 67.7, and 106.8 $\mu\text{g}/\text{cm}^2$ are denoted by asterisks, open triangles, open circles, open squares, and open diamonds, respectively. (b) The data for He gas with thicknesses of 15.7, 29.3, 59.2, 124.0, and 247.1 $\mu\text{g}/\text{cm}^2$ are denoted by asterisks, open triangles, open circles, open squares, and open diamonds, respectively. (c) The data for N_2 gas with thicknesses of ~ 10 , ~ 40 , ~ 800 , and ~ 1200 $\mu\text{g}/\text{cm}^2$ are denoted by asterisks, open triangles, open circles, and open squares, respectively. The charge distribution in N_2 gas at equilibrium was not obtained accurately.

The fraction of the charge state q_i was calculated as described in a previous study [36]; this charge state fraction is defined as

$$F(q_i) = \frac{1}{N} \frac{I_{J33}/q_i}{I_{X51}/q_{\text{ini}}}, \quad (2)$$

where N denotes a normalization constant, I_{X51} and I_{J33} denote the beam intensities measured at FC-X51 and FC-J33, respectively, and q_{ini} denotes the incident charge state of 20+. The index i extends over the range of possible charge states of 0–36. In order to determine N , an unnormalized fraction $f(q_i) = \frac{I_{J33}/q_i}{I_{X51}/q_{\text{ini}}}$ was firstly calculated. The data set of $f(q_i)$ is fitted by a Gaussian function. However, the beam transmission efficiency was only 3% in this study, and the beam intensity measured with each Faraday cup includes its own offset value; hence, the sum $\sum f(q_i)$ over all i does not equal unity. Therefore, the area of the fitted Gaussian function is calculated and introduced as the normalization constant N in order to obtain the sum of $F(q_i)$ as unity. Subsequently, the set of $F(q_i)$ is fitted by a Gaussian function again. The error bars in the fraction data $F(q_i)$ in Fig. 11 are attributed to the uncertainty of the normalization constant N , which is arising from the errors of the fitting parameters.

The most probable charge states are defined as the central values obtained via the fitting procedure. However, as the gas thickness increases, the discrepancy between $F(26+)$ and $F(27+)$ is significant, as clearly shown in Fig. 11(a). It is known as the *shell effect*, first observed by Moak *et al.* [45], and also observed in the case of uranium stripping [34]. This discrepancy is caused by the difficulty of ionizing from the L shell of the Kr ion. Ionization potentials to remove one M-shell electron from Kr^{25+} and one L-shell electron from Kr^{26+} are 1.2 keV and 2.9 keV, respectively [46]. The electron traveling with projectile with kinetic energy of 2.7 MeV/nucleon ($\beta = 0.076$) has a kinetic energy of 1.5 keV. It is difficult to strip electrons with removal energies higher than 1.5 keV [47,48]. This fact also implies that excited states have little contribution in ionization process in gases [45]. Thus, the standard Gaussian function cannot reproduce the charge distribution. Consequently, an asymmetric parameter ϵ_a is introduced to improve the fitting results, as described in Ref. [28]. The corresponding asymmetric Gaussian function is written as

$$F_a(q) = F_{\text{mp}} \exp \left[-\frac{t^2}{2(1 + \epsilon_a t)} \right], \quad (3)$$

$$t = \frac{q - q_{\text{mp}}}{\sigma}, \quad (4)$$

where q , q_{mp} , F_{mp} , and σ denote the charge state, the most probable charge state, fraction at the most probable charge state, and distribution width, respectively. Fitting by both standard and asymmetric Gaussian functions were applied in the case that the fraction values $F(26+)$ and $F(27+)$ were both greater than zero. The asymmetric Gaussian was adopted when the reduced chi-square value became smaller than the result of the standard Gaussian. The fitted parameters for the H_2 and He charge strippers are listed in Table I along with their uncertainties. The thickness is calculated for H_2 , He , and N_2 gases by the linear functions obtained in Sec. III B. The errors in thickness are attributed to the uncertainties of the fitting parameters. The most probable charge states correspond to the mean charge states in the case of the standard Gaussian for which the asymmetric factor $\epsilon_a = 0$. The mean charge states are slightly less than the most probable charge states if the asymmetric factor is less than zero. We found that the mean charge states in H_2 and He gases attain equilibrium at 25.1 and 23.2, respectively. The charge state of ^{86}Kr in N_2 at equilibrium was estimated to be less than 20+. Further, we could obtain a Kr^{26+} beam with a charge fraction of 31% in H_2 for a thickness of 68 $\mu\text{g}/\text{cm}^2$; thus, H_2 gas is a good candidate for Kr-ion acceleration. For practical usage, the amount of the fraction $F(26+)$ is sufficient at the H_2 gas thickness of 70 $\mu\text{g}/\text{cm}^2$, which corresponds to the required P_1 pressure of 0.7 kPa. On the assumption that the aperture of 10 mm in diameter can be applied to practical operation,

TABLE I. Fitting parameters of ^{86}Kr charge state distributions using H_2 and He gas charge strippers. The listed errors are attributed to the fitting procedure.

Pressure (kPa)	Thickness ($\mu\text{g}/\text{cm}^2$)	Peak height	Mean charge state	Distribution width (σ)	Asymmetric factor (ϵ_a)
H_2					
0.11	10.3 ± 1.0	0.262 ± 0.008	22.13 ± 0.07	1.52 ± 0.08	0
0.23	22.7 ± 2.1	0.268 ± 0.007	23.73 ± 0.05	1.49 ± 0.05	0
0.47	45.6 ± 4.2	0.336 ± 0.011	24.75 ± 0.07	1.16 ± 0.05	-0.25 ± 0.06
0.70	67.7 ± 6.3	0.368 ± 0.009	25.06 ± 0.05	1.06 ± 0.03	-0.23 ± 0.04
1.10	106.8 ± 9.9	0.359 ± 0.010	25.07 ± 0.06	1.09 ± 0.03	-0.25 ± 0.06
He					
0.085	15.7 ± 1.5	0.238 ± 0.003	21.98 ± 0.04	1.67 ± 0.04	0
0.16	29.3 ± 2.7	0.233 ± 0.004	22.70 ± 0.03	1.72 ± 0.04	0
0.32	59.2 ± 5.5	0.250 ± 0.004	23.21 ± 0.04	1.59 ± 0.03	-0.07 ± 0.03
0.67	124.0 ± 11.5	0.256 ± 0.004	23.16 ± 0.04	1.55 ± 0.03	-0.12 ± 0.03
1.34	247.1 ± 22.8	0.258 ± 0.006	22.90 ± 0.04	1.54 ± 0.05	0

the required pumping speeds should be greatly enhanced to maintain the pressure at each stage as same as this study. Especially, the required pumping speed for the second stage is estimated to be over $10000 \text{ m}^3/\text{h}$. As a realistic solution, the second stage would be divided into two stages (stage 2 and 3) evacuated by MBPs, and hence the next stage (stage 4) would be evacuated by TMP. The required pumping speeds for stages 2, 3, and 4 are $4000 \text{ m}^3/\text{h}$ (MBP), $2000 \text{ m}^3/\text{h}$ (MBP), and $5400 \text{ m}^3/\text{h}$ (TMP), respectively. However, since the full length of the system becomes long, the suitable design of a beam transport is also needed.

The equilibrium charge states in H_2 and He are plotted in Fig. 12 along with the data shown in Fig. 2. The solid and open squares represent the Q_{eq}/Z values of H_2 and He ,

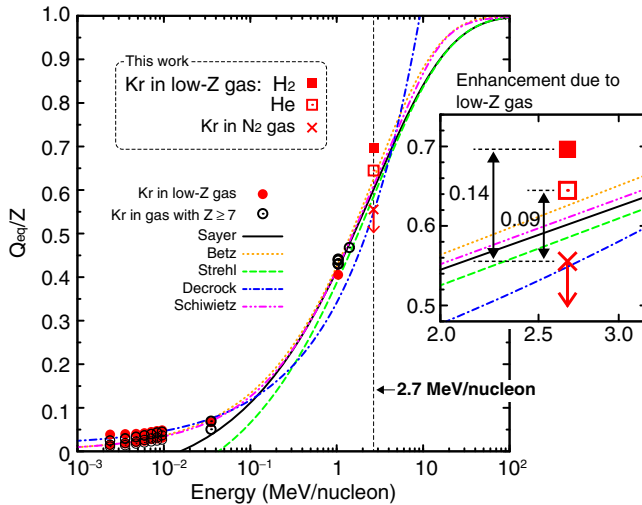


FIG. 12. Q_{eq} data for Kr ions in gas media including results of this work. The solid and open squares indicate Q_{eq}/Z values of ^{86}Kr in H_2 and He gases, respectively. The x-mark represents the Q_{eq}/Z value in N_2 based on the assumption that Q_{eq} equals $20+$. Q_{eq}/Z in N_2 is actually estimated to be smaller (i.e., Q_{eq}/Z will shift along the direction of the arrow).

respectively, as obtained in this study. The x-mark represents the Q_{eq}/Z value for N_2 on the assumption that Q_{eq} in N_2 equals $20+$. The Q_{eq}/Z values were enhanced by 0.14 and 0.09 in H_2 and He gases, respectively, when compared with the case of N_2 gas. Their enhancements of Q_{eq} can be larger since Q_{eq} in N_2 is actually estimated to be smaller (i.e., Q_{eq}/Z for N_2 will shift along the direction of the arrow in Fig. 12).

V. CHARGE STATE CALCULATIONS

In general, the reactions causing a change in the charge are divided into two categories: ionization and electron capture. The equilibrium charge state is determined by the competing processes of ionization and electron capture. Ionization can result from collisions between projectile electrons and the target nuclei or bound electrons. Electron capture can occur by the transfer of electrons from the target atoms to the projectile. The details regarding the calculations of the ionization and electron capture cross sections are summarized in Ref. [49], and further, the consistency between the theoretical and experimental cross sections is also demonstrated. In this section, we use the CGS system of units following the description in Ref. [49].

A. Ionization reactions

A semi-classical approach to Born-based calculations that is classified under the set of *binary encounter model* (BEM) has been developed for simplified application to ionization calculations. These models were proposed first by Gryzinski [50] and Garcia [51]. Additional work toward their development was performed by Vriens [52]. Calculations based on this model employ a simplified two-body Coulomb scattering cross section for the target nuclear charge collision with the projectile electrons. The cross section for the ionization of an electron in the nl shell (nl -electron) in the projectile is defined as

$$\sigma_{nl} = 4\pi a_0^2 \left(\frac{\text{Ry}}{I_{nl}} \right)^2 (\bar{Z}_t^2 + Z_t) G(V), \quad (5)$$

where $G(V)$ denotes the function of the scaled velocity $V = v/v_{nl}$ in which v and v_{nl} represent the incident velocity of the projectile and the velocity of the nl -electron, respectively. If $V > 0.206$, the value of the function is given by:

$$G(V) = \frac{\alpha^{3/2}}{V^2} (1-\beta)(1-\beta^{1+V^2}) \left\{ \alpha + \frac{2}{3}(1+\beta)\ln(2.7+V) \right\} \quad (6)$$

with

$$\alpha = \frac{V^2}{1+V^2} \quad \text{and} \quad \beta = \frac{1}{4V(1+V)}; \quad (7)$$

for $V < 0.206$, $G(V)$ is simply

$$G(V) = \frac{4V^4}{15}. \quad (8)$$

The constant $4\pi a_0^2 \text{Ry}^2$ gives $4\pi a_0^2 \text{Ry}^2 = 6.51 \times 10^{-14} \text{ (cm}^2 \text{ eV}^2\text{)}$, where Ry denotes the Rydberg unit of energy $\text{Ry} = 13.6 \text{ (eV)}$ and a_0 the Bohr radius $a_0 = 5.29 \times 10^{-9} \text{ (cm)}$. The parameter I_{nl} represents the ionization potential experienced by the nl -electron in the projectile, and Z_t denotes the target nuclear charge. The values of I_{nl} are available at the NIST homepage [46].

The term \bar{Z}_t denotes the effective screened target nuclear charge as perceived by the individual nl -electron in the projectile. For the sake of simplicity, \bar{Z}_t is temporarily denoted by $\bar{Z}_t(b_{nl})$, where b_{nl} denotes an impact parameter experienced by the projectile nl -electron. The expression for $\bar{Z}_t(b_{nl})$ is given by

$$\bar{Z}_t(b_{nl}) = Z_t - \int_0^{b_{nl}} n(r) d^3r, \quad (9)$$

where $n(r)$ denotes the electron density about the target nucleus at a given radius r . The simplified approach to obtain $n(r)$ is discussed in Ref. [49], and from the approach, we have

$$n_n(r) = \frac{C_n}{r} \exp\left(-\frac{r}{B_n}\right), \quad (10)$$

where $n_n(r)$ denotes the density of electrons in shell n (n -electrons), and C_n and B_n denote the parameters determined for each shell n . The parameters C_n and B_n are expressed using the total number of n -electrons, N_n , as below

$$N_n = 4\pi C_n B_n^2. \quad (11)$$

B_n can be interpreted as the median radius of a given shell n , and it is obtained from the definition in Ref. [49],

$$B_n = \frac{n^2 a_0}{Z_t - S_n}, \quad (12)$$

where S_n denotes the screening value for the n -electrons in the target. S_n is determined as

$$S_n \approx f_i N_i + f_n N_n + f_o N_o, \quad (13)$$

where f_i , f_n , and f_o denote the fractions of the inner electrons N_i , n -electrons N_n , and outer electrons N_o enclosed within B_n , respectively. The values of f_i , f_n , and f_o applied in Ref. [49] are 0.90, 0.264, and 0.10, respectively. Consequently, here, the total electron density is given by

$$n(r) = \sum_n n_n(r). \quad (14)$$

The relation between the impact parameter and ionization potential is given by

$$I_{nl} = \frac{\bar{Z}_t(b_{nl}) e^2}{b_{nl}}, \quad (15)$$

where e denotes the elementary charge. The impact parameter b_{nl} is obtained by solving Eqs. (9) and (15) for b_{nl} . We derive $\bar{Z}_t(b_{nl})$ by substituting the obtained b_{nl} value in Eq. (9).

Following Bethe [53] and Scheidenberger *et al.* [54], the contribution of the target-bound electrons to the total ionization cross section can be incorporated by using the term $\bar{Z}_t^2 + Z_t$ in Eq. (5). The ionization cross sections are functions of the square of the ionizing charge. The term \bar{Z}_t^2 represents an interaction between the nl -electron in the projectile and the ionizing charge \bar{Z}_t . In the case of interaction between the nl -electron in the projectile and an electron in the target atom, the square of the electron charge is unity, but it contributes by a factor of Z_t to the cross section. The total ionization cross section σ^{BEM} can be calculated by summation over all nl -electrons in the projectile as

$$\sigma^{\text{BEM}} = \sum_{nl} \sigma_{nl}. \quad (16)$$

B. Electron capture reactions

The capture of an electron in a target by a projectile ion can occur either by a radiative or a nonradiative reaction. Radiative capture reactions dominate over nonradiative capture in the energy range higher than 100 MeV/nucleon [54]. In the energy region studied here, the cross sections corresponding to the radiative process contribute less than 10^{-2} of the total capture cross section. The significant nonradiative process for target electron capture by a projectile is the *charge transfer* reaction. The first model of the charge transfer reaction is attributed to

Oppenheimer [55], and it was later refined by Brinkman and Kramers [56]. The final form is known as the OBK model. This charge transfer reaction rate depends on the initial energy E_i of the bound electron in the target and its final energy E_f in the projectile ion, where E_i and E_f denote the binding energy in the initial and final states, characterized by the quantum numbers n_i and n_f , respectively. The charge transfer cross section is expressed by

$$\sigma^{\text{OBK}} = 4.1 \times 10^4 \sum_{n_i} \sum_{n_f} N_i a_{\text{eik}} \times \frac{Q_p^2 e^4 E_i^{\frac{5}{2}} E_f^{\frac{3}{2}} E_k^4}{\{E_k^2 + 2E_k(E_i + E_f) + (E_i - E_f)^2\}^5} \quad (17)$$

in which $E_k = m_e v_e^2/2$, where m_e and v_e denote the electron mass and velocity, respectively, Q_p the projectile charge state, and N_i the number of electrons in the original target shell with a quantum number n_i . The eikonal factor a_{eik} accounts for reduction in this reaction with increased deviation from the Born approximation on which it is based. This factor is expressed as

$$a_{\text{eik}} = \frac{\pi \eta v_i}{\sinh(\pi \eta v_i)} \exp \left[-2\eta v_i \arctan \left(\frac{v - \epsilon \eta}{v_i} \right) \right] \quad (18)$$

where $\eta = \alpha_{\text{fs}} c/v$ (α_{fs} : fine-structure constant), $\epsilon = (E_f - E_i)/Ry$, and $v_i = \sqrt{E_i/Ry}$. The total charge transfer reaction rate is obtained by summing over all the initial electron bound states in the target and all final captured states in the projectile.

C. Relation between cross sections and equilibrium charge states

The total ionization σ^{BEM} and electron capture σ^{OBK} cross sections are plotted as functions of the projectile charge state in Fig. 13. The total ionization and electron capture cross sections of Kr in H_2 gas are represented by solid and dash-two-dotted curves, respectively. The ionization and electron capture cross sections in He gas are represented by dash-dotted and dotted curves, respectively. For these curves, we followed the calculation procedure described in Ref. [49]. The charge state at the intersection point represents the predicted value of the equilibrium charge state. The predicted equilibrium charge states for H_2 and He gases are 25.01 and 23.43, respectively. In fact, the experimentally obtained mean charge states at equilibrium are slightly lower than these predicted values due to energy loss in the gas.

As described in Refs. [49,57], in certain cases, the calculated cross sections differ from the experimental results by a factor of 2 or more. Therefore, we introduce parameters a and b , which are optimized such that the calculation of the charge state evolution reproduces the experimental data. The ionization cross section σ^{ion} and

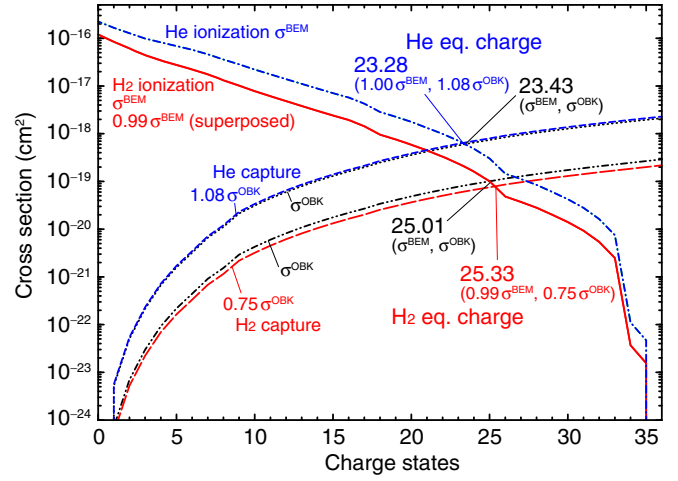


FIG. 13. Total ionization and capture cross sections for 2.7-MeV/nucleon ^{86}Kr penetrating H_2 and He targets. The ionization and electron capture cross sections (σ^{BEM} and σ^{OBK}) of Kr in H_2 gas are represented by solid and dash-two-dotted curves, respectively. The ionization and electron capture cross sections in He gas are represented by dash-dotted and dotted curves, respectively. The charge states at the intersection point for H_2 and He are 25.01 and 23.43, respectively. Ionization and electron capture cross sections optimized to fit the experimental data of mean charge states ($a\sigma^{\text{BEM}}$ and $b\sigma^{\text{OBK}}$) are also plotted as a function of the projectile charge states. The solid and long-dashed curves indicate the cross sections multiplied by $a_{\text{H}_2} = 0.99$ and $b_{\text{H}_2} = 0.75$ for H_2 . The dash-dotted and dotted curves represent cross sections multiplied by $a_{\text{He}} = 1.00$ and $b_{\text{He}} = 1.08$ for He. The charge states at the intersection point are 25.33 and 23.28 for H_2 and He gases, respectively.

electron capture cross section σ^{cap} are defined using Eqs. (16) and (17), as follows:

$$\sigma^{\text{ion}} = a\sigma^{\text{BEM}}, \quad (19)$$

$$\sigma^{\text{cap}} = b\sigma^{\text{OBK}}. \quad (20)$$

1. Evolution of charge state distribution

When an ion beam passes with a velocity v through a target of thickness t , the charge state composition of the beam varies due to ionization and electron capture events. In our study, the fractions of the charge state q were defined as the function $Y_q(t)$ at each thickness value t . The fractions $Y_q(t)$ obey a system of linear coupled differential equations,

$$\frac{dY_q(t)}{dt} = \sum_{q \neq q'} [\sigma(q', q)Y_{q'}(t) - \sigma(q, q')Y_q(t)], \quad (21)$$

where $\sigma(q, q')$ denotes the cross sections for changing the charge state from q to q' . The summation in Eq. (21) is extended by q and q' over the range of possible charge

states. The fractions Y are normalized by $\sum_q Y_q = 1$. Here, with the assumption that the charge changing process occurs via single-electron loss or capture, i.e., $|q' - q| = 1$, Eq. (21) yields the following simple relation upon using the notations σ^{ion} and σ^{cap} ,

$$\begin{aligned} \frac{dY_q(t)}{dt} = & \sigma^{\text{ion}}(q-1, q)Y_{q-1}(t) \\ & - \{\sigma^{\text{cap}}(q, q-1) + \sigma^{\text{ion}}(q, q+1)\}Y_q(t) \\ & + \sigma^{\text{cap}}(q+1, q)Y_{q+1}(t). \end{aligned} \quad (22)$$

Equation (22) is integrated over the thickness t by the Runge-Kutta-Gill method, and the mean charge state q_m is calculated as $q_m^{\text{cal}} = \sum_q q Y_q$ for each thickness listed in Table I. The parameter χ^2 is defined as $\chi^2 \equiv \sum_{i=1}^{n_{\text{exp}}} \left(\frac{q_{m,i}^{\text{exp}} - q_{m,i}^{\text{cal}}}{\delta_i} \right)^2$ where $q_{m,i}^{\text{exp}}$ and δ_i are the experimentally obtained mean charge states listed in Table I and their uncertainties, respectively, and index i ranges from 1 to the total number of data points ($n_{\text{exp}} = 5$ for both H_2 and He gas measurements).

The parameters a and b in Eqs. (19) and (20) were fitted such that the χ^2 value becomes minimum. The obtained values of a and b were 0.99 and 0.75 for H_2 and 1.00 and 1.08 for He, respectively. The optimized ionization and electron capture cross sections are shown in Fig. 13. The ionization and electron capture cross sections are multiplied by $a_{\text{H}_2} = 0.99$ and $b_{\text{H}_2} = 0.75$ for H_2 , and $a_{\text{He}} = 1.00$ and $b_{\text{He}} = 1.08$ for He gas, respectively. The solid and long-dashed curves in Fig. 13 indicate the optimized cross sections for H_2 . The dash-dotted and dashed curves in Fig. 13 indicate those for He. The charge states at the point of intersection are 25.33 and 23.28 for H_2 and He gas, respectively.

Figure 14 shows the mean charge states plotted as a function of the gas thickness. The horizontal error bars represent the thickness uncertainty listed in Table I. The uncertainties in the mean charge state are smaller than the symbols. The calculation results obtained using the optimized parameters a and b are also indicated by solid and dotted curves for H_2 and He gases, respectively. The calculation results obtained using the optimized parameter sets $(a_{\text{H}_2}, b_{\text{H}_2})$ and $(a_{\text{He}}, b_{\text{He}})$ are represented by solid and dotted curves for H_2 and He gases, respectively. In addition, the data corresponding to the C-foil [23] are also indicated by solid triangles for comparison.

The charge state distributions reproduced by calculations using the optimized cross sections are shown in Figs. 15 and 16 for H_2 and He, respectively. Figures 15(a), (b), (c), (d), and (e) show the charge distributions in H_2 for thicknesses of 106.8, 67.7, 45.6, 22.7, and 10.3 $\mu\text{g}/\text{cm}^2$, respectively. The solid circles represent the data shown in Fig. 11(a). The solid lines

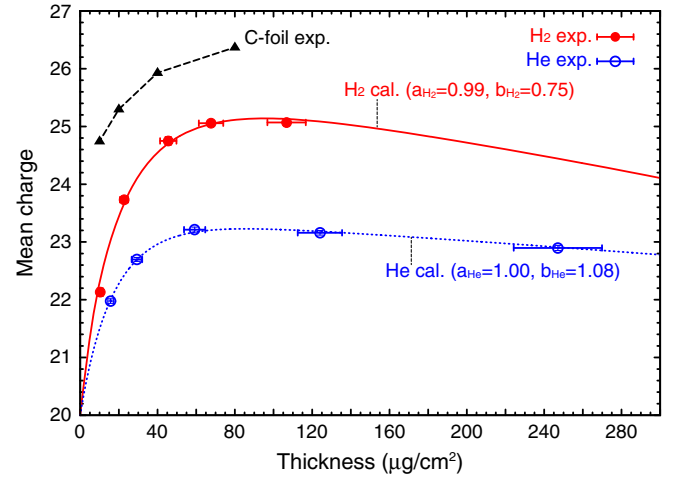


FIG. 14. Mean charge states of ^{86}Kr plotted as a function of gas thickness. The data for H_2 and He gases are represented by solid and open circles, respectively. The data corresponding to the C-foil stripper are also indicated by solid triangles. The calculation results obtained using the optimized parameter sets $(a_{\text{H}_2}, b_{\text{H}_2})$ and $(a_{\text{He}}, b_{\text{He}})$ are represented by solid and dotted curves for H_2 and He gases, respectively.

represent the calculated results with optimized parameters $a_{\text{H}_2} = 0.99$ and $b_{\text{H}_2} = 0.75$. Figures 16(a), (b), (c), (d), and (e) represent the charge distributions in He for thicknesses of 247.1, 124.0, 59.2, 29.3, and 15.7 $\mu\text{g}/\text{cm}^2$, respectively. The solid circles represent the data shown in Fig. 11(b). The solid lines represent the calculated results with the optimized parameters $a_{\text{He}} = 1.00$ and $b_{\text{He}} = 1.08$.

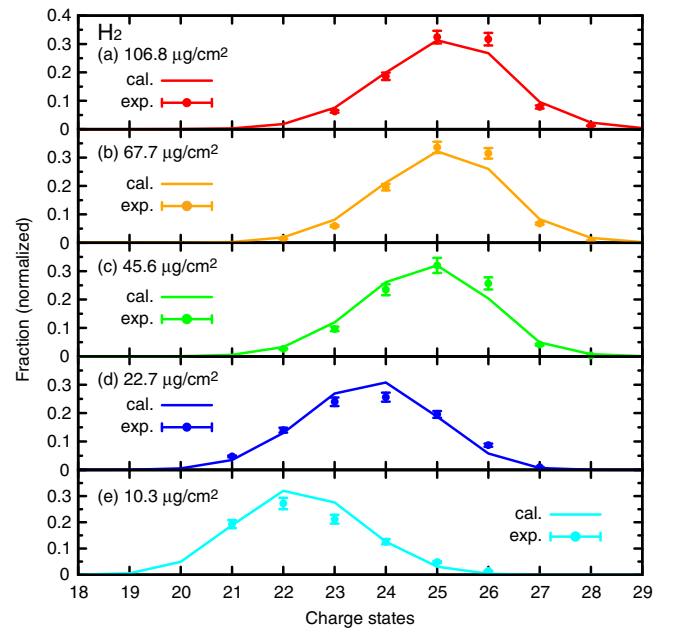


FIG. 15. The charge state distribution of ^{86}Kr in H_2 for various thicknesses. The charge distributions at thicknesses of (a) 106.8, (b) 67.7, (c) 45.6, (d) 22.7, and (e) 10.3 $\mu\text{g}/\text{cm}^2$ are indicated by solid circles along with the calculated fractions (solid lines).

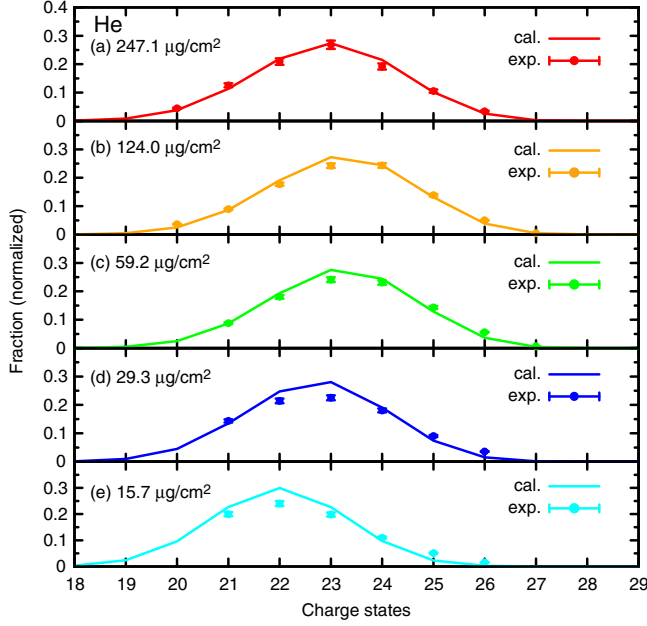


FIG. 16. The charge state distribution of ^{86}Kr in He for various thicknesses. The charge distributions at thicknesses of (a) 247.1, (b) 124.0, (c) 59.2, (d) 29.3, and (e) 15.7 $\mu\text{g}/\text{cm}^2$ are indicated by solid circles along with the calculated fractions (solid lines).

2. Distribution width

The widths of the charge distributions for low- Z gas strippers are narrow comparing with those of N_2 gas, as described in Sec. IV A. The distribution width can be calculated as written in Refs. [16,58], once the adequate cross sections for ionization and electron capture are obtained. The ionization and electron capture cross sections can be partially presented by exponential form:

$$\sigma^{\text{ion}}(q, q+1) = \sigma_0^{\text{ion}} \exp[-c_i(q - q_0)], \quad (23)$$

$$\sigma^{\text{cap}}(q, q-1) = \sigma_0^{\text{cap}} \exp[c_c(q - q_0)], \quad (24)$$

where $\sigma^{\text{ion}}(q, q+1)$ and $\sigma^{\text{cap}}(q, q-1)$ denote the ionization and electron capture cross section at the charge state q , respectively, σ_0^{ion} and σ_0^{cap} denote constants, c_i and c_c are fitting parameters with positive values ($c_i, c_c > 0$), and q_0 is the charge state at the intersection point, which corresponds to the predicted equilibrium charge state as described at the beginning of this section. If $F(q)$ is the fraction of charge q , the fractions $F(q)$ and $F(q+1)$ have the relation,

$$F(q)\sigma^{\text{ion}}(q) = F(q+1)\sigma^{\text{cap}}(q+1), \quad (25)$$

and similarly,

$$F(q-1)\sigma^{\text{ion}}(q-1) = F(q)\sigma^{\text{cap}}(q). \quad (26)$$

Substituting q_0 into q , the following relations are obtained using Eqs. (23)–(26),

$$\frac{F(q_0+1)}{F(q_0)} = \frac{\sigma_0^{\text{ion}}}{\sigma_0^{\text{cap}}} \exp(-c_c), \quad (27)$$

$$\frac{F(q_0-1)}{F(q_0)} = \frac{\sigma_0^{\text{cap}}}{\sigma_0^{\text{ion}}} \exp(-c_i). \quad (28)$$

On the assumption that the charge distribution has standard Gaussian form, the relation $F(q_0+1)/F(q_0) = F(q_0-1)/F(q_0)$ can be obtained. We derive

$$\sigma_0^{\text{ion}} = \sigma_0^{\text{cap}} \exp\left[\frac{1}{2}(-c_i + c_c)\right]. \quad (29)$$

Substituting Eq. (29) into Eq. (27),

$$\frac{F(q_0+1)}{F(q_0)} = \exp\left[-\frac{1}{2}(c_i + c_c)\right]. \quad (30)$$

On the other hand, the fraction of each charge state is calculated by a Gaussian function,

$$F(q) = F(q_0) \exp\left[-\frac{(q - q_0)^2}{2\sigma_{\text{cal}}^2}\right], \quad (31)$$

where σ_{cal} denotes the calculated width. For $q = q_0 + 1$, we obtain the relation

$$\frac{F(q_0+1)}{F(q_0)} = \exp\left[-\frac{1}{2\sigma_{\text{cal}}^2}\right]. \quad (32)$$

Comparing Eqs. (30) and (32), we obtain σ_{cal} as

$$\sigma_{\text{cal}} = \sqrt{\frac{1}{c_i + c_c}}. \quad (33)$$

The σ_{cal} is calculated assuming that each mean charge state listed in Table I is considered as q_0 . Firstly, σ^{ion} and σ^{cap} in the forms of Eqs. (23) and (24) are calculated for q_0 from the cross sections optimized in Sec. V C 1. The parameters c_i and c_c are obtained by the fitting to the cross sections around q_0 . Then the σ_{cal} is calculated from Eq. (33). Figure 17 shows the distribution width σ in Table I along with σ_{cal} as a function of the gas thickness. The data for H_2 and He gases are represented by solid and open circles, respectively. The calculation results of σ_{cal} obtained using the optimized parameter sets ($a_{\text{H}_2}, b_{\text{H}_2}$) and ($a_{\text{He}}, b_{\text{He}}$) are represented by solid and dashed curves with asterisks and x-marks for H_2 and He gases, respectively. The values of σ_{cal} for H_2 well reproduced the measured widths, although the calculation is based on the assumption that the charge state distribution attains at equilibrium. Those of He gas are in agreement within an accuracy of 0.2 at the thickness sufficient for equilibrium. It is found that the distribution width at the equilibrium can be reproduced by the accurate

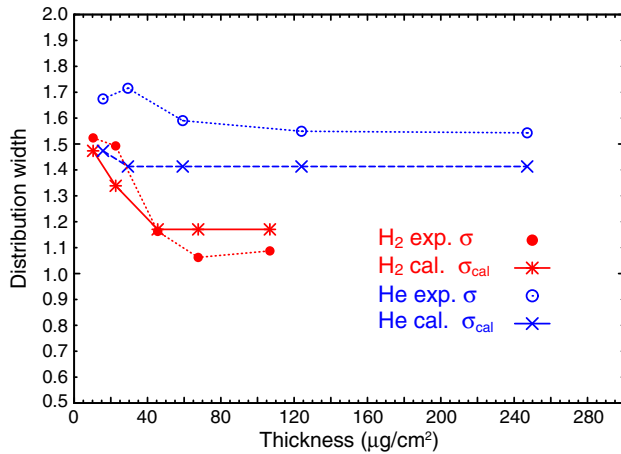


FIG. 17. The distribution width σ in Table I and the calculated width σ_{cal} are plotted as a function of gas thickness. The data for H_2 and He gases are represented by solid and open circles, respectively. The calculation results of σ_{cal} using the optimized parameter sets (a_{H_2} , b_{H_2}) and (a_{He} , b_{He}) are represented by solid and dashed curves with asterisks and x-marks for H_2 and He gases, respectively. The σ_{cal} for H_2 well reproduced the measured widths. Those of He gas are in agreement within an accuracy of 0.2 at the thickness sufficient for equilibrium.

ionization and electron capture cross sections, without calculations of the charge evolution as described in Sec. VC 1.

VI. SUMMARY AND CONCLUSIONS

We measured the charge state distributions of ^{86}Kr at 2.7 MeV/nucleon by using H_2 and He gas charge strippers. The mean charge states of ^{86}Kr in H_2 and He gases attained equilibrium at 25.1 and 23.2, respectively, whereas the mean charge state in N_2 gas at equilibrium was estimated to be below 20. The Q_{eq}/Z values were enhanced by 0.14 and 0.09 in H_2 and He gases, respectively. We were able to obtain $^{86}\text{Kr}^{26+}$ with a fraction of 31% in H_2 gas with a thickness of 68 $\mu\text{g}/\text{cm}^2$. The H_2 gas stripper can be applied for ^{86}Kr acceleration. The ionization and electron capture cross sections calculated by using the BEM and OBK model were optimized such that the calculation of the charge state evolution reproduced the experimental data. The optimized scaling factors a and b are $a = 0.99$ and $b = 0.75$ for H_2 and $a = 1.00$ and $b = 1.08$ for He.

ACKNOWLEDGMENTS

The authors are grateful to the RILAC operation crews for providing high-quality beams and for their assistance in the experimental preparations and measurements. The authors would like to thank the cyclotron operation crews for tuning the beams downstream of the RILAC. The authors also acknowledge the constructive suggestions and advice from Dr. Uwamino relating to safety management on the use of hydrogen gas.

- [1] FRIB, <http://www.frib.msu.edu>.
- [2] FAIR, <https://www.gsi.de/en/research/fair.htm>.
- [3] SPIRAL2, <http://www.ganil-spiral2.eu>.
- [4] G. Robert-Demolaize *et al.*, in *Proceedings of the 5th International Particle Accelerator Conference (IPAC 2014), Dresden, Germany, 2014* (JACoW, Dresden, Germany, 2014), p. 1090.
- [5] P. N. Ostroumov *et al.*, in *Proceedings of the 25th Particle Accelerator Conference (PAC 2013), Pasadena, CA, 2013* (IEEE, New York, 2013), p. 737 (2013).
- [6] Y. Yano, *Nucl. Instrum. Methods Phys. Res., Sect. B* **261**, 1009 (2007).
- [7] H. Okuno, N. Fukunishi, and O. Kamigaito, *Prog. Theor. Exp. Phys.* **2012**, 3C002 (2012).
- [8] T. Nakagawa, Y. Higurashi, M. Kidera, T. Aihara, M. Kase, and Y. Yano, *Nucl. Instrum. Methods Phys. Res., Sect. B* **226**, 392 (2004).
- [9] M. Odera, Y. Chiba, T. Tonuma, M. Hemmi, Y. Miyazawa, T. Inoue, T. Kambara, M. Kase, T. Kubo, and F. Yoshida, *Nucl. Instrum. Methods Phys. Res.* **227**, 187 (1984).
- [10] Y. Yano, in *Proceedings of the 13th International Cyclotron Conference*, (World Scientific, Singapore, 1992), p. 102.
- [11] M. Kase, E. Ikezawa, N. Fukunishi, O. Kamigaito, H. Okuno, M. Kidera, H. Ryuto, T. Nakagawa, M. Komiyama, N. Sakamoto *et al.*, in *Proceedings of the 17th International Conference on Cyclotrons and Their Applications* (Particle Accelerator Society of Japan, Tokyo, Japan, 2004), p. 160.
- [12] J. Ohnishi, M. Fujimaki, N. Fukunishi, A. Goto, K. Ikegami, O. Kamigaito, M. Kase, K. Kumagai, M. Nagase, H. Okuno *et al.*, in *Proceedings of the 17th International Conference on Cyclotrons and Their Applications* (Particle Accelerator Society of Japan, Tokyo, Japan, 2004), p. 197.
- [13] H. Okuno, J. Ohnishi, N. Fukunishi, T. Tominaka, K. Ikegami, A. Goto, T. Fujinawa, M. Nagase, H. Ryuto, S. Yokouchi *et al.*, in *Proceedings of the 17th International Conference on Cyclotrons and Their Applications* (Particle Accelerator Society of Japan, Tokyo, Japan, 2004), p. 373.
- [14] H. Okuno, K. Yamada, J. Ohnishi, N. Fukunishi, K. Ikegami, T. Maie, H. Hasebe, O. Kamigaito, N. Sakamoto, K. Kumagai *et al.*, *IEEE Trans. Appl. Supercond.* **18**, 226 (2008).
- [15] H. Hasebe, M. Kase, H. Ryuto, and Y. Yano, in *Proceedings of the 17th International Conference on Cyclotrons and Their Applications* (Particle Accelerator Society of Japan, Tokyo, Japan, 2004), p. 313.
- [16] H. Betz, *Rev. Mod. Phys.* **44**, 465 (1972).
- [17] E. Baron, *IEEE Trans. Nucl. Sci.* **19**, 256 (1972).
- [18] A. Wittkower and H. Betz, *Atomic Data* **5**, 113 (1973).
- [19] B. Erb, GSI Report No. P-7-78, 1978.
- [20] K. Shima, T. Mikumo, and H. Tawara, *At. Data Nucl. Data Tables* **34**, 357 (1986).
- [21] A. Leon, S. Melki, D. Lisfi, J. Grandin, P. Jardin, M. Suraud, and A. Cassimi, *At. Data Nucl. Data Tables* **69**, 217 (1998).
- [22] A. Fettouhi, H. Weick, M. Portillo, F. Becker, D. Boutin, H. Geissel, R. Knöbel, J. Kurcewicz, W. Kurcewicz, J. Kurpeta *et al.*, *Nucl. Instrum. Methods Phys. Res., Sect. B* **245**, 32 (2006).

- [23] H. Hasebe (unpublished).
- [24] H. Ryuto, N. Fukunishi, H. Hasebe, N. Inabe, S. Yokouchi, O. Kamigaito, A. Goto, M. Kase, and Y. Yano, in *Proceedings of the 21st Particle Accelerator Conference, Knoxville, TN, 2005* (IEEE, Piscataway, NJ, 2005), p. 3751.
- [25] N. Bohr and J. Lindhard, *K. Dan. Vidensk. Selsk. Mat. Fys. Medd.* **28**, 7 (1954).
- [26] H. Betz and L. Grodzins, *Phys. Rev. Lett.* **25**, 211 (1970).
- [27] G. Maynard, M. Chabot, D. Gardès, C. Schmelzer, B. Stadler, and J. Wehrauch, *Nucl. Instrum. Methods Phys. Res., Sect. B* **164–165**, 139 (2000).
- [28] R. Sayer, *Rev. Phys. Appl.* **12**, 1543 (1977).
- [29] H. Betz, *Applied Atomic Collision Physics* (Academic, New York, 1983), Vol. 4, p. 1.
- [30] P. Strehl, *Handbook of Accelerator Physics and Engineering*, 2nd ed. (World Scientific, Singapore, 1999), p. 555.
- [31] P. Decrock, E. Kanter, and J. Nolen, *Rev. Sci. Instrum.* **68**, 2322 (1997).
- [32] G. Schiwietz and P. Grande, *Nucl. Instrum. Methods Phys. Res., Sect. B* **175–177**, 125 (2001).
- [33] R. Clark, I. Grant, R. King, D. Eastham, and T. Joy, *Nucl. Instrum. Methods Phys. Res.* **133**, 17 (1976).
- [34] H. Imao, H. Okuno, H. Kuboki, S. Yokouchi, N. Fukunishi, O. Kamigaito, H. Hasebe, T. Watanabe, Y. Watanabe, M. Kase *et al.*, *Phys. Rev. ST Accel. Beams* **15**, 123501 (2012).
- [35] A. Perumal, V. Horvat, R. Watson, Y. Peng, and K. Fruchey, *Nucl. Instrum. Methods Phys. Res., Sect. B* **227**, 251 (2005).
- [36] H. Kuboki, H. Okuno, S. Yokouchi, H. Hasebe, T. Kishida, N. Fukunishi, O. Kamigaito, A. Goto, M. Kase, and Y. Yano, *Phys. Rev. ST Accel. Beams* **13**, 093501 (2010).
- [37] H. Kuboki, H. Okuno, H. Hasebe, S. Yokouchi, N. Fukunishi, Y. Higurashi, J. Ohnishi, T. Nakagawa, H. Imao, O. Kamigaito *et al.*, *Phys. Rev. ST Accel. Beams* **14**, 053502 (2011).
- [38] H. Okuno, N. Fukunishi, A. Goto, H. Hasebe, H. Imao, O. Kamigaito, M. Kase, H. Kuboki, Y. Yano, and S. Yokouchi, *Phys. Rev. ST Accel. Beams* **14**, 033503 (2011).
- [39] K. Sagara, A. Motoshima, T. Fujita, H. Akiyoshi, and N. Nishimori, *Nucl. Instrum. Methods Phys. Res., Sect. B* **378**, 392 (1996).
- [40] T. Kishida, Y. Gono, M. Shibata, H. Watanabe, T. Tsutsumi, S. Motomura, E. Ideguchi, X. Zhou, T. Morikawa, T. Kubo *et al.*, *Nucl. Instrum. Methods Phys. Res., Sect. A* **438**, 70 (1999).
- [41] Hakuto Co. Ltd., <http://www.hakuto-vacuum.jp/> and the instruction manuals.
- [42] T. Watanabe, N. Fukunishi, M. Kase, M. Wakasugi, M. Fujimaki, K. Yamada, N. Sakamoto, Y. Kotaka, R. Koyama, T. Nakamura *et al.*, in *Proceedings of the 7th Annual Meeting of Particle Accelerator Society of Japan*, (Particle Accelerator Society of Japan, Himeji, Hyogo, Japan, 2010), p. 1029.
- [43] J. Lindhard and A. Sorensen, *Phys. Rev. A* **53**, 2443 (1996); ATIMA site: <http://web-docs.gsi.de/~weick/atima/>.
- [44] O. Tarasov and D. Bazin, *Nucl. Instrum. Methods Phys. Res., Sect. B* **266**, 4657 (2008); LISE site: <http://www.nsl.mscl.edu/lise>.
- [45] C. Moak, H. Lutz, L. Bridwell, L. Northcliffe, and S. Datz, *Phys. Rev. Lett.* **18**, 41 (1967).
- [46] National Institute of Standards and Technology (NIST), Nist atomic spectra database ionization energy form, <http://physics.nist.gov/PhysRefData/ASD/ionEnergy.html>.
- [47] N. Bohr, *K. Dan. Vidensk. Selsk. Mat. Fys. Medd.* **18**, 8 (1948).
- [48] K. Shima, N. Kuno, and M. Yamanouchi, *Phys. Rev. A* **40**, 3557 (1989).
- [49] M. S. Armel, Ph.D. thesis, University of California at Berkeley, 2000.
- [50] M. Gryzinski, *Phys. Rev.* **138**, A305 (1965).
- [51] J. Garcia, *Phys. Rev. A* **1**, 280 (1970).
- [52] C. Vriens, in *Proceedings of the Royal Society* (London, GB, 1966), Vol. 90, p. 935.
- [53] H. Bethe, *Ann. Phys. (Berlin)* **397**, 325 (1930).
- [54] C. Scheidenberger, T. Stöhlker, W. Meyerhof, H. Geissel, P. Mokler, and B. Blank, *Nucl. Instrum. Methods Phys. Res., Sect. B* **142**, 441 (1998); GLOBAL codes accessible as utilities in LISE ++, <http://groups.nsl.mscl.edu/lise/>.
- [55] J. Oppenheimer, *Phys. Rev.* **31**, 349 (1928).
- [56] H. Brinkman and H. Kramers, *Proc. Acad. Sci. Amsterdam* **33**, 973 (1930).
- [57] D. Mueller, L. Grisham, I. Kaganovich, R. Watson, V. Horvat, K. Zaharakis, and M. Armel, *Phys. Plasmas* **8**, 1753 (2001).
- [58] G. Bell, *Phys. Rev.* **90**, 548 (1953).